Vortex merging and splitting: a route to elasto-inertial turbulence in Taylor-Couette flow

T. Lacassagne and S. Balabani*
Department of Mechanical Engineering, University College London (UCL), London, WC1E 7JE, UK

N. Cagney
School of Engineering and Materials Science, Queen Mary University of London

J.J.J. Gillissen
Department of Mathematics, University College London (UCL), London, WC1E 6BT, UK
(Dated: September 28, 2020)

We report experimental evidence of a new merge-split transition (MST) to elasto-inertial turbulence (EIT) in Taylor-Couette flows of viscoelastic polymer solutions, caused by merging and splitting of base Taylor vortices when crossed by elastic axial waves (rotating standing waves, RSW). These vortex merging and splitting events are not due to transient behaviour, finite aspect ratio or shear thinning behaviour. They are random in nature and increase in frequency with Re; when superimposed on a RSW flow state they cause abrupt changes in the axial spatial wavelength, leading to the transition from a RSW to the EIT state. We thus identify MST as an inertial feature solely triggered by elasticity and independent of any shear-thinning behaviour.

I. INTRODUCTION

Taylor-Couette flow (TCF) is the flow in the gap between two concentric cylinders with one or both rotating. Such flows have many practical applications in rheology or mixing [1, 2]. Over the past century [3], they have also served as a great tool for the fluid mechanics community to study various flow instabilities induced by complex fluids. Indeed, with the inner cylinder rotated and the outer cylinder fixed, the purely azimuthal Couette-flow (CF) is known to destabilize when a critical rotation speed is reached, leading to the flow transitioning to the so called Taylor Vortex Flow (TVF). In Newtonian fluids a variety of steady and unsteady flow states already exists [4] depending on the Reynolds number (Re) defined as

$$Re = \rho \Omega r_i d/\mu \tag{1}$$

where ρ is the fluid density, Ω the rotation speed, r_i the inner cylinder radius and d the gap width. Alternatively, the Taylor number $Ta = \rho\Omega\sqrt{r_i d^3}/\mu$ can also be used to describe the CF to TVF transition.

When the fluid in the gap is non Newtonian, more complex flow transitions can emerge, in particular when the fluid displays elastic properties.

In the absence of inertia (vanishing Re), elastic fluids exhibit a CF-TVF transition induced by a purely elastic instability [5]. As elasticity increases, the flow exhibits a chaotic behaviour, which is referred to as elastic turbulence [6, 7]. A hysteretic behaviour can also be observed, in which diwhirls appear when the inner cylinder decelerates under conditions that would produce a purely azimuthal flow during acceleration [8–10].

In the presence of inertia (higher Re), elastic fluids are subject to elasto-inertial instabilities, leading to the existence of non-axisymmetric flow states such as ribbons (RIB) [11] or rotating standing waves (RSW) [10, 12, 13]. Gradual transitions from such flows to elasto-inertial turbulence (EIT), through a series of increasingly chaotic flow states, have been reported in the literature [13, 14].

Notably, in shear-thinning and elastic polyethylene-oxide solutions, an interesting *defect* behaviour of the RIB spirals has been observed [11]. It has been shown that the multiplications of such defects when increasing the rotation speed of the inner cylinder lead to the flow transitioning to EIT, through a process called *defect mediated turbulence* (DMT) [11].

In the present work we report experimental evidence of a new merge-split transition (MST) to EIT, caused by merging and splitting of base Taylor vortices (abrupt changes in the axial spatial wavelength) when crossed by axial RSW waves. We identify MST as an inertial feature solely triggered by elasticity, independent of any shear-thinning behaviour. It should be noted that the diwhirls previously observed [9, 10], also correspond to an hysteresis in the number of vortices, but occur only during deceleration of the inner cylinder.

* s.balabani@ucl.ac.uk

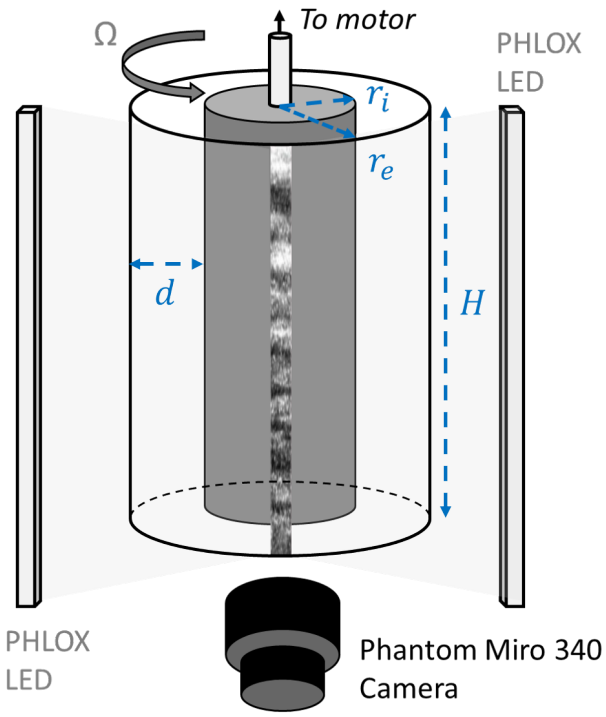

Figure 1. Schematic of the experimental set-up showing the Taylor-Couette cell and the visualisation arrangement

II. EXPERIMENTS

Here we perform ramp-up (slow acceleration of the inner cylinder) and steady state experiments (constant rotation speed of the inner cylinder) in a purely elastic Boger fluid made of 200 ppm PAAM (polyacrylamide, Sigma-Aldrich, $M_w = 5.5 \times 10^6$ g.mol^{-1}) dissolved in a 28% water 72% glycerol mixture. The flow cell (figure 1) comprised a transparent acrylic outer cylinder and nylon inner cylinder spray-painted with black non reflective paint to avoid spurious light reflections and ensure smoothness of the rotating surface. Alignment between inner and outer cylinder was ensured by a ball bearing and a notch complementing the inner cylinder's conical end, at the top and bottom lid respectively. The cylinder was driven from the top using a stepper motor (SmartDrive Ltd, Cambridge, U.K.), the rotation of which could be controlled to a high degree of precision by a 52 000 microstep/revolution controller (SmartDrive Ltd, Cambridge, U.K.).

The top and bottom lids were stationary, with a ~ 3 mm gap between lid and cylinder at both ends. The inner chamber, which was completely filled with working fluid (no free surface), had an axial length of $H = 155$ mm, and the inner and outer radii were 21.66 mm and 27.92 mm, respectively. This corresponds to a gap width of $d = 6.26$ mm, a radius ratio of $\eta = r_i/r_o = 0.77$, and an aspect ratio $AR = H/d = 21.56$ (figure 1). The cell was enclosed in a rectangular chamber in which water was recirculated via a temperature bath to ensure that the temperature of the working fluid remained constant at 20°C throughout the experiments.

The shear-rheology was measured using a rotational rheometer (ARES, TA Instruments) equipped with a Couette geometry (inner radius 32 mm, outer radius 34 mm), in steady shear mode. A constant viscosity of $\mu = 0.0481$ Pa.s was found (figure 2 a). The elastic properties of the working fluid were assessed through oscillatory shear experiments on the same rheometer and geometry. The evolution of elastic and viscous moduli G' and G" respectively with oscillation frequency is measured in the linear deformation region (1% strain). G" values were corrected by removing the contribution of the solvent viscosity, $\mu_s = 0.0419$ Pa.s, such that $\tilde{G}$" $= G$" $- \mu_s\omega$ and the elastic time scale is defined as $t_e = 2\pi/\omega_c$ where ω_c is the crossover point between $\tilde{G}$" and G' curves [15] (see figure 2 b)). The measured elastic time-scale is $t_e = 0.2110$ s and the elastic number is $El = t_e\mu/\rho d^2 = 0.2263$, with $\rho = 1198$ kg.m^{-3}. Rheological characterization of the working fluid before and after the experiments gave similar results, indicating negligible polymer degradation.

The flow was visualized by adding a small amount of reflective mica flakes, at a volume fraction of the order of 10^{-4} (0.01%), sufficiently low not to disturb the flow [16], and illuminating them using two LED stripes (PHLOX White led Linear light 260) arranged as shown in figure 1. The flakes' response time is defined as $t_f = (l^2\rho)/\mu$, where l is the flakes' equivalent diameter ranging from about 10 μm to 100 μm. t_f was found to be at least two orders of magnitude smaller than the fastest time-scales of the flow. Images of the flow were acquired by a Phantom Miro 340 camera,

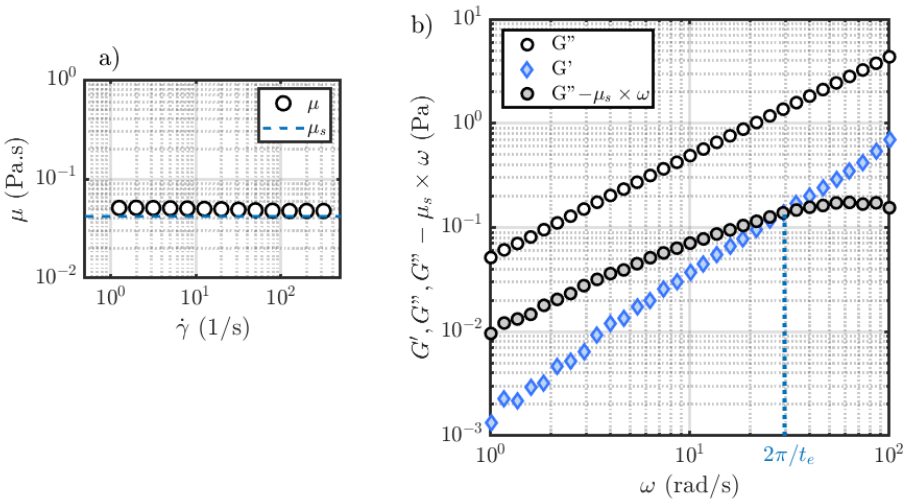

Figure 2. Oscillatory shear rheological characterisation of the working fluid (1% strain). The elastic time-scale is obtained by removing the contribution of the solvent viscosity μ_s to G" curves as $\tilde{G}" = G" - \mu_s \times \omega$, and finding the crossover between G' and $\tilde{G}"$ (vertical dashed line)

along a narrow strip in the axial dimension (vertical), at 90 fps and 900 fps for ramp up and steady state experiments, respectively. For ramp up experiments, this corresponds to a Reynolds number increment of $\Delta Re = 0.007$ between two successive frames. The 2176×16 pixels images (135 mm $\times$0.994 mm) are averaged in the azimuthal direction to form an axial intensity profile for each instant/Reynolds number. All profiles are compiled into a matrix, or flow map showing the evolution of the flow structures with time or Reynolds number (e.g figure 3 b), 4).

Flow maps are divided into shorter time sequences (256 successive times, 50% overlap) in order to calculate the average Fast Fourier Transform (FFT) for each row in each sequence. All the averaged spectra are then compiled to form a frequency map. This map shows the evolution of the characteristic frequencies of the flow as a function of time or Reynolds number [17] (e.g figure 3 c)).

For the ramp up experiments, the inner cylinder rotation speed Ω is slowly increased at a constant rate, $\mathrm{d}\Omega/\mathrm{d}t$, up to a maximum value Ω_{max}. For steady state experiments, the rotation speed (and hence Reynolds number) is held constant during the recording time following a slow ramp up phase. In both cases, the acceleration rate, defined as $\Gamma_0 = \frac{\mathrm{d}Re}{\mathrm{d}t^*} = \frac{\rho^2 r_i d^3}{\mu^2}\frac{\mathrm{d}\Omega}{\mathrm{d}t}$, is kept below unity ($\Gamma_0 = 0.3312$). This is commonly used as a criterion to ensure that transient, acceleration related effects can be neglected [18]. The values of $\mathrm{d}\Omega/\mathrm{d}t$ and the corresponding Γ_0 were chosen as a best compromise to achieve quasi-steady ramp up while avoiding polymer chain destruction. Experiments at higher acceleration rate ($\Gamma_0 \sim 10$) have also been conducted, and the flow map remained unaffected.

III. RESULTS

A. Ramp up

Figure 3 shows the results of the ramp up experiment, that allows the flow transitions to be monitored over a continuous range of Re. The flow state succession is the following: CF-TVF-RSW-EIT. This set of transitions is expected in purely elastic Boger fluids [12]. In sub-figure 3 a) the rms of the flow map intensity along z is shown as a function of Re. This allows the critical Re for transition from CF to TVF to be identified at $Re_{c1} = 80$. This gives a $Re^*_{c1} = Re_{c1}/Re^0_{c1} = 0.88$ where $Re^0_{c1} = 92.3$ is the critical Reynolds number in an inelastic Newtonian fluid (same solvent without PAAM) measured in the same experimental setup. The TVF to RSW transition is clearly evidenced from the sudden appearance of a number of ridges in the frequency map (figure 3 c) corresponding to the typical frequencies of the RSW state. This second transition occurs at $Re_{c2} = 88$, $Re^*_{c2} = Re_{c2}/Re^0_{c1} = 0.95$. We note that the frequencies of these ridges stay constant with increasing Re throughout the RSW state during ramp up(figure 3 c).

Even more remarkably, the k harmonic frequencies of the RSW ridges can be written as $f^k = k \times f_e$ where $f_e = 2c_e/\lambda$ is the elastic wave frequency based on the elastic wave celerity $c_e = \sqrt{\mu/(\rho t_e)}$ [7, 19] (assuming that the spatial wavelength is $\lambda \simeq d$, see figure 8). The first 3 dominant f^k frequencies, found at $k = [\frac{1}{3}, \frac{2}{3}, 1]$ are evidenced

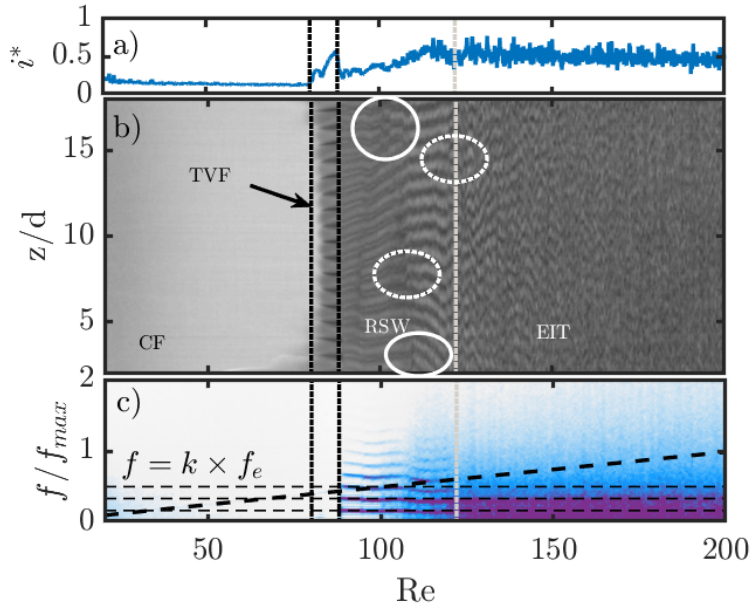

Figure 3. Reynolds-space and frequency-space diagrams of the ramp up experiment. a) z root mean square i^* of the b) Reynolds-space flow map intensity, such that $i^*(Re) = \langle I(z, Re)\rangle_{\mathrm{rms,z}}$ with I the gray-scale intensity of flow map 3 b). c) Frequency map where the frequency axis is scaled by the maximum inner cylinder frequency reached at the end of the experiment, $f_{max} = 2\pi/\Omega_{max} = 9.45$ Hz. Vertical black dotted lines denote transitions from CF to TVF and to RSW states. The more gradual transition from RSW to EIT is also illustrated by a vertical gray dotted line. The cylinder frequency increase with Re is illustrated with the black dashed line. Horizontal dashed lines matching RSW state frequency ridges are plotted at $f = k \times f_e$, $k = [\frac{1}{3}, \frac{2}{3}, 1]$.

by the horizontal dashed lines of figure 3 c). Finally, the RSW state gradually transitions to EIT from $Re_{c3} \simeq 122$ ($Re^*_{c3} = Re_{c3}/Re^0_{c1} = 1.3$) onwards. The previous flow state succession is consistent with the experiments of Groisman and Steinberg [12] even though TVF would have been expected to transition directly to EIT at the present El value. The discrepancy may be attributed to differences in the radius ratio ($\eta = 0.71$ in [12]). Some merging and splitting events, highlighted in figure 3 b) by full and dotted circles respectively, can be observed in the RSW state, confirming that such events can be observed in quasi-steady ramp-up experiments.

B. Steady-state experiments

In figure 4, steady state experiments performed at four different Reynolds numbers are reported. Note that while the RSW state can be seen in the ramp up experiment at $Re = 94$, it corresponds to a clear TVF state in the steady state experiments. This is not surprising given the general sensitivity of non-Newtonian Taylor-Couette flows to experimental conditions.

In the TVF regime (S1, figure 4 a,e), no merging or splitting occurs over a 50 s time span, and the Taylor vortices are steady. The RSW state (S2, S3, figure 4 b,c,f,g) is characterised by a base Taylor vortex flow with axial oscillations corresponding to axial waves, namely the "rotating spiral waves" [12]. Merging and splitting events (highlighted by full and dotted line ellipses respectively) are clearly evidenced there. In S3, merging and splitting events involving more than 2 vortex pairs are also observed. Note that some vortices appear to drift in or out of the map at the top or bottom, where they merge with or separate from the Ekman vortices respectively. Details on two selected examples of splitting and merging in the RSW state are shown in figure 4 i) and j) respectively. The EIT state (S4, figure 4 d,h) appears as an extremely unsteady RSW state, where tracks of the base Taylor vortices are still visible but submerged in strong axial flow oscillations and frequent merging and splitting of multiple vortices simultaneously.

Figure 4 proves that MST does not require shear-thinning as in DMT [11]), and is not an effect of a transient behaviour due to the finite Γ_0 value. They occur in a purely elastic fluid, and during steady state experiments.

A schematic representation of the MST mechanism is provided in figure 5 (in the (θ,z) plane), illustrating the role of asymmetric RSW waves in merging and splitting vortices and vortex pairs.

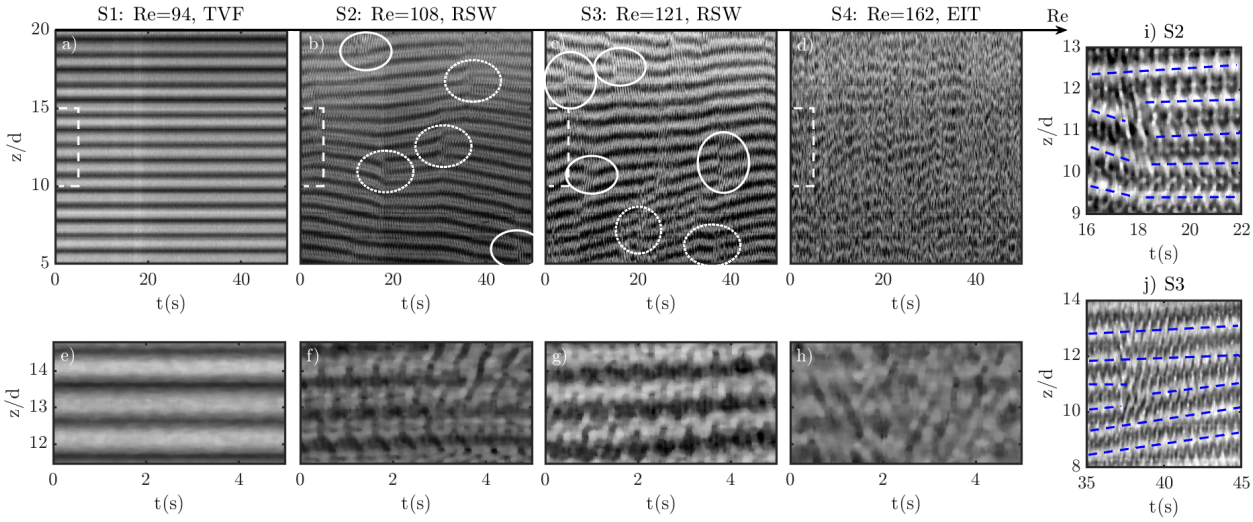

Figure 4. Steady state recordings at constant Re of successive RSW and EIT states. (a-d) Time-space diagrams over 50 s time spans. (e-h) Detailed section of the same flow maps on the first 5 seconds and in the central region (dashed rectangles). Merging and splitting of Taylor vortices in the RSW flow state are indicated by full and dotted line ellipses respectively. Note that the EIT flow state is essentially composed of a high number of indistinguishable merging and splitting along with axial oscillations. i) and j) are detailed close-up on splitting (i, S2, $t = 18$ s) and merging (j, S3, $t = 38$ s) events (RSW), where dashed lines are guide to the eye showing the base Taylor vortices.

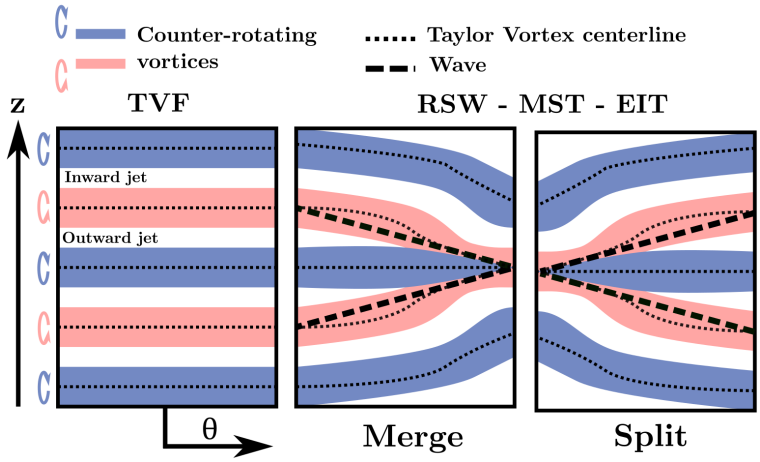

Figure 5. Role of RSW waves in the merging and splitting of Taylor vortices, illustrated in the unwrapped (θ,z) plane. Only a central vertical line of this plane is sampled to produce flow maps shown in figures 3 and 4, as explained in figure 1.

C. Space and time spectra

To provide further quantitative description of the observed flow states, frequency spectra of steady state experiments (FFT of intensity time series at a given Re) are shown in figure 6 a), where the frequency axis is scaled by the elastic wave frequency f_e. Frequency spectra of various flow states are also extracted along vertical lines of figure 3 c), and plotted in figure 6 b), with the frequency axis normalized as $2\pi f/\Omega$. The spectra confirm the behaviour observed also in the flow and frequency maps (figure 3), namely that the RSW state is a superposition of waves of various frequencies, several of which have comparable amplitudes, and that this combination of waves transitions to EIT upon increasing Re [11]. One of the RSW spectral peaks corresponds to $f = f_e$, where f_e is the elastic wave frequency [7, 12, 19], as also seen in figure 3 c). The most energetic peaks are found for k sub-harmonics of f_e such that $f^k = k \times f_e$, with $k = 1/3$ and $k = 2/3$. When Re is increased, the peaks become less discernible, and the frequencies appear slightly shifted towards lower values on figure 6 b), as Ω increases with Re while the elastic relaxation frequency f_e stays constant.

The spectra clearly illustrate the progressive transition from the RSW state to EIT as the discrete coherent oscilla-

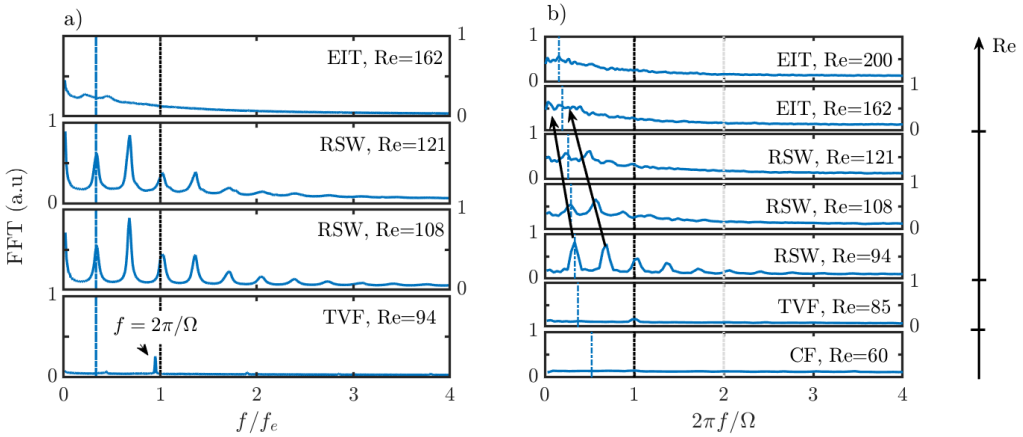

Figure 6. Evolution with Re of the frequency spectra of flow states obtained from steady state experiments (a), and extracted from the frequency map in figure 3 c) (b). Frequencies (x axis) are scaled by the elastic frequency f_e on a) and by the cylinder's rotation frequency $\Omega/2\pi$ on b). In subfigure b), vertical black and gray dotted lines denote this latter frequency and its first harmonic respectively. Vertical mixed blue lines are plotted at $f = \frac{1}{3}f_e$. In sub-figure a) vertical dotted and mixed lines denote the $f = f_e$ and $f = \frac{1}{3}f_e$ peaks respectively.

tions of the RSW state, the frequencies of which do not depend on Re but rather correspond to the elastic frequency, merge into a continuous broadband [12, 13] spectrum, consistent with the flow maps of figures 3 and 4. This latter spectrum (upper pannel in figure 6 b) is similar to that of turbulent Taylor-Couette flows in Newtonian fluids [2, 20, 21], thus justifying the name of "elasto-inertial turbulence" or "elasticity dominated turbulence" [13, 14].

To further investigate the role of merging and splitting events in this RSW to EIT transition, the axial spatial wavelength is computed for each vertical slice (Re) of the time-space or Re-space diagrams in figures 3 b) or 4. This is achieved by taking the FFT of the intensity signal along the axial dimension z, and finding the dominant peak frequency, which is simply the inverse of the spatial wavelength, as illustrated in figure 7 a). In doing so, one allows the wavelength to vary without being constrained to rational numbers (e.g the height divided by the number of vortex pairs), thus accounting for the gradual merging, splitting or drift of vortices (see figures 4, 8, 7).

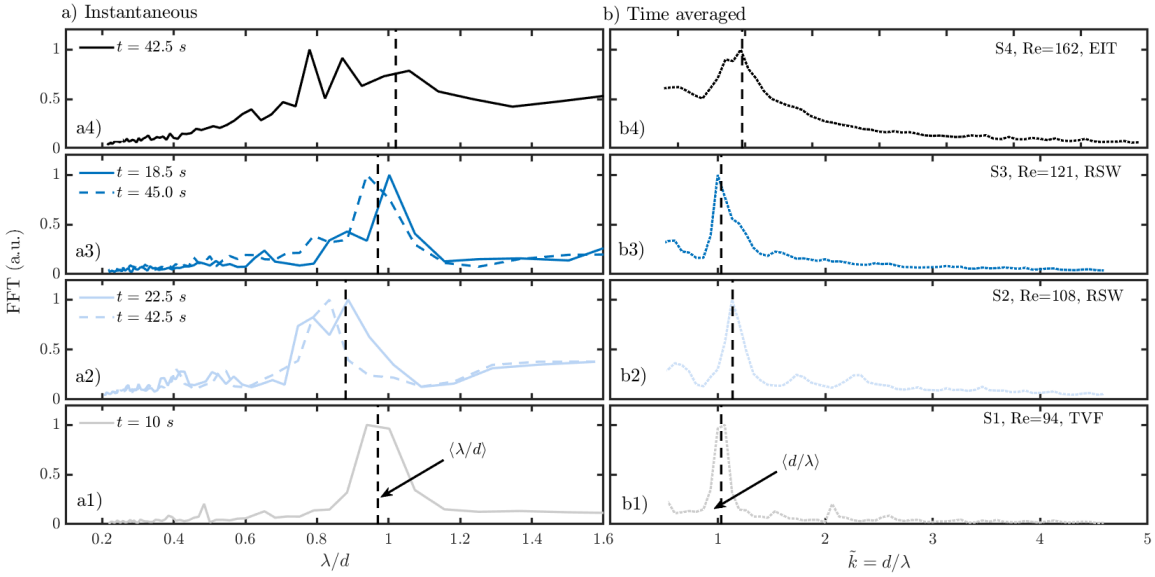

.

Figure 7. a) Instantaneous and b) time-averaged spatial spectra (Fourier transform on intensity profiles in the axial direction) of steady state experiments as a function of the normalized wave-length λ/d (a) and normalized wave number $\tilde{k} = d/\lambda$ (b)

Figure 7 shows examples of spatial Fourier transform of the intensity profile along the axial direction z, for steady state experiments. Note that band-pass filtering is applied to suppress frequencies lower than $10/H$ and higher than $100/H$ (with H the height of the flow cell). This is equivalent to assuming that the number of vortices in the test

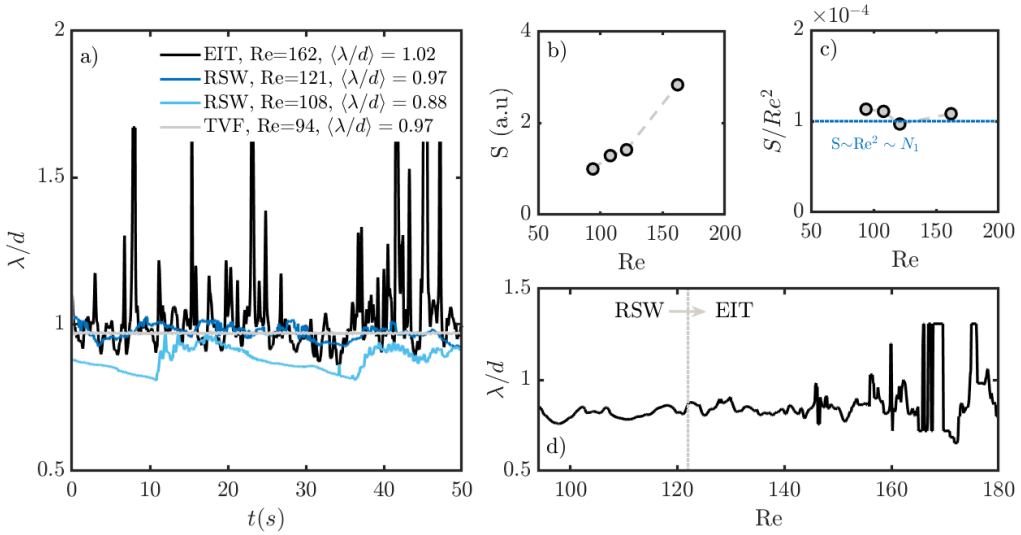

Figure 8. Axial spatial wavelength λ/d, expressed as a function of time for steady state experiments (a), and as a function of Re for the ramp up experiment (d). b) Shows the evolution of normalized standard deviation S of λ/d on the full duration of each steady state experiment as a function of Re. c) evidences the $S \sim Re^2 \sim N_1$ scaling by plotting S/Re^2 as a function of Re.

section is between 10 and 100, which can be checked visually on figures 2 and 3.

In sub-figures a) (a1 to a4), instantaneous spectra are plotted as a function of the normalized wavelength λ/d. Two instantaneous spectra (a2, a3) are shown for the RSW state cases to illustrate the wavelength drift due to merging and splitting. In sub-figures b) (b1 to b4), time averaged spectra are plotted as a function of the normalized wave number $\tilde{k} = d/\lambda$. The vertical dashed lines illustrate the time averaged wavelength $\langle\lambda/d\rangle$ or time averaged wave number $\langle d/\lambda\rangle$ on a) and b) respectively (vertical dashed lines). In figure 7 a) merging and splitting of Taylor vortices lead to a drift of the instantaneous wavelength in RSW and EIT states. In figure 7 b) the time averaged spectra show a wave number peak consistent with the time averaged wave number $\langle d/\lambda\rangle$ (see also figure 8).

In the absence of vortex merging and splitting, the wavelength stays constant in the TVF case. Variations of λ of the two RSW cases (S2, S3, see figure 4) are of similar amplitude but even more gradual and random for the higher Re of the two. They are a consequence of a more complex combination of merging, splitting and drift. This effect is further enhanced in the EIT case (figure 8 a, dark curve). The wavelength fluctuates around its time averaged value $\langle\lambda/d\rangle$ reported in figure 8 a. This nominal wavelength varies between 0.88 and 1.02 among all steady-state experiments.

The amplitude of fluctuations S is related to vortex merging and splitting events, and is plotted in figure 8 b). It is quantified for all experiments as the normalized standard deviation of any λ/d time series, denoted $std(\lambda/d)$, divided by the standard deviation of the λ/d times series in TVF, denoted $std(\lambda/d)_{TVF}$, such that

$$S = \frac{std(\lambda/d)}{std(\lambda/d)_{TVF}}. \tag{2}$$

S values increase with increasing Re, *i.e* with increasing the probability of merging and splitting events, as shown in figure 8 b). The dependency on Re appears to be quadratic, as illustrated by figure 8 c). The reason for this scaling discussed in section IV. Finally λ/d is shown as a function of Re for the ramp up experiment in figure 8 d). The gradual transition from RSW to EIT corresponds to increased noise in the main spatial wavelength.

Figure 9 finally displays plots of spatio-temporal spectra (two-dimensional FFT) for steady state experiments S2 (a) and S4 (b). Temporally averaged spectra (as previously reported in figure 6) are projected on the a2 and b2 planes. Spatially averaged spectra (as previously reported in figure 7) are projected on the a3 and b3 planes. The spectra intensities are rescaled in arbitrary units. Figure 9 allows to evidence the correlation between spatial and temporal frequencies in the RSW state, and how this behaviour turns to a broadband chaos in the EIT state, both in time and space.

Despite the broadband spectral behaviour, EIT is here found at relatively low Re values for which no turbulence would exist in a Newtonian fluid. The structure of EIT is thus likely to be different from that of so-called viscoelastic turbulence, in which inertial turbulent scaling laws are modified by the presence of polymers [22]. Further investigation

using time resolved quantitative flow velocity measurements in the gap, such as particle image velocimetry [17], could allow to characterise the structure of transitional EIT.

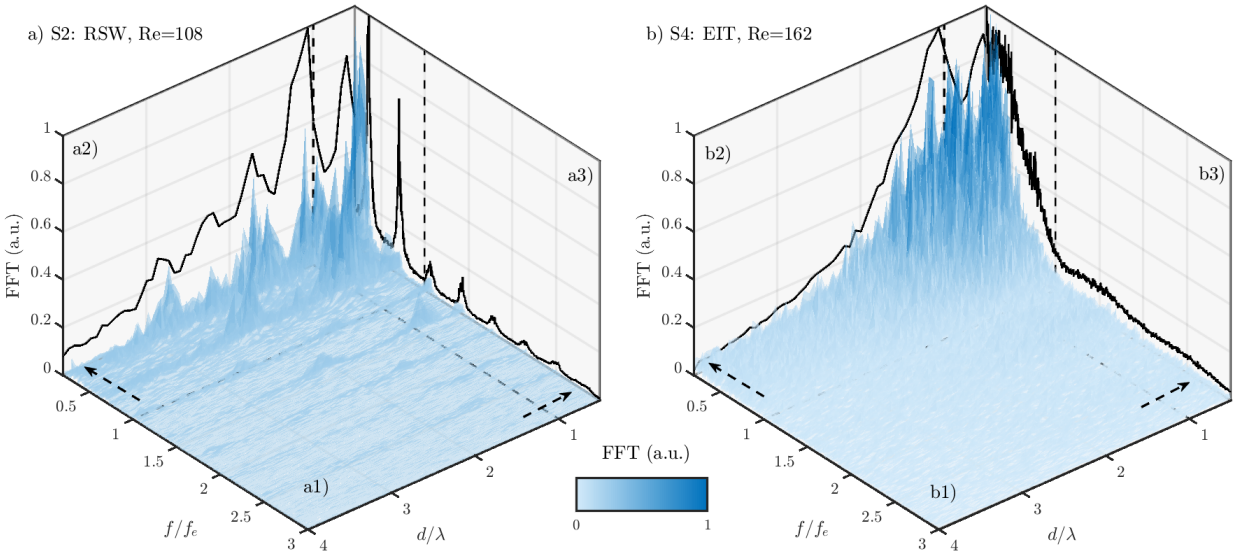

Figure 9. Spatio-temporal spectra obtained by two-dimensional FFT in RSW (a) and EIT (b) steady state experiments. Spatially averaged spectra are projected in planes a3 and b3. Temporally averaged spectra are projected in planes a2 and b2. Projections are indicated by dashed arrows.

IV. DISCUSSION AND CONCLUSION

The fact that the RSW oscillation frequencies are Re-independent and related to the elastic time-scale of the polymer solution show that the RSW state originates from the elastic features of the fluid. RSW is thus an inertial mode modified by elastic effects [12], and such effects induce a transition to elasto-inertial turbulence. It is generally known that multiple periodic elastic waves may superimpose to generate randomness and transition to elastic [6] or elasto-inertial turbulence [13, 19, 23]. The latter phenomenon is also observed here, with RSW transitioning to EIT.

In an elastic Taylor-Couette flow, polymer molecules are stretched by the strong base azimuthal flow and release energy into the transverse secondary flow. Such a polymer relaxation energy transfer is believed to be the origin of axial elastic waves in the RSW state [12]. This argument is also consistent with the early (elastic) onset of the TVF primary instability, attributed to the normal stress difference of elastic polymeric solutions [5], and to direct numerical simulations findings on elasto-inertial Taylor-Couette turbulence by [14].

The same physical mechanisms are likely to be responsible for the existence and increased occurrence with Re of merging and splitting events. The first normal stress difference N_1 scales with the square of the shear rate $\dot{\gamma}$ [12, 24]. Defining $\dot{\gamma} = \Omega r_i/d$ in a Taylor-Couette flow of a constant viscosity fluids [17], we obtain

$$N_1 = 2\mu t_e \left(\Omega \frac{r_i}{d}\right)^2 \tag{3}$$

Combining equations 1 and 3, and for a given constant viscosity μ, one gets $N_1 \sim Re^2$. Here in figure 8 c), it appears that a $S \sim Re^2 \sim N_1$ scaling satisfactorily describes the increase of merging and splitting probability upon Re or N_1 increase.

As a final note, the fact that vortex merging and splitting occur in a Boger fluid (constant viscosity) during a steady state experiment (no transient ramp-up effects) broadly suggests that this behaviour is not due to the transient nature of the ramp up process or to shear-thinning. Experimental evidence herein supports the view that it is triggered by axial waves, as exist in RSW state. Interpretation of the results in terms of normal stress thus suggests that it is associated with fluid elasticity. Such abrupt wavelength changes prove to be one of the features leading to the observation of EIT, when occurring repeatedly on top of a RSW flow state. This can be described as a merge-split elasto-inertial transition to turbulence (MST).

ACKNOWLEDGEMENTS

Financial support for this work from the Engineering and Physical Sciences Research Council (EPSRC) Manufacturing the Future programme (No.EP/N024915/1) is gratefully acknowledged.

---

[1] M. A. Fardin, C. Perge, and N. Taberlet, "The hydrogen atom of fluid dynamics" – introduction to the Taylor–Couette flow for soft matter scientists, Soft Matter **10**, 3523 (2014).

[2] S. Grossmann, D. Lohse, and C. Sun, High–Reynolds Number Taylor-Couette Turbulence, Annual Review of Fluid Mechanics **48**, 53 (2016).

[3] G. I. Taylor, Stability of a viscous liquid contained between two rotating cylinders, Philosophical Transactions of the Royal Society of London. Series A, Containing Papers of a Mathematical or Physical Character **223**, 289 (1923).

[4] C. Andereck, S. Liu, and H. Swinney, Flow regimes in a circular Couette system with independently rotating cylinders, Journal of Fluid Mechanics **164**, 155 (1986).

[5] R. G. Larson, E. S. G. Shaqfeh, and S. J. Muller, A purely elastic instability in Taylor–Couette flow, Journal of Fluid Mechanics **218**, 573 (1990).

[6] S. Berti and G. Boffetta, Elastic waves and transition to elastic turbulence in a two-dimensional viscoelastic Kolmogorov flow, Physical Review E **82**, 036314 (2010).

[7] A. Varshney and V. Steinberg, Elastic Alfven waves in elastic turbulence, Nature Communications **10**, 1 (2019).

[8] A. Groisman and V. Steinberg, Solitary Vortex Pairs in Viscoelastic Couette Flow, Physical Review Letters **78**, 1460 (1997).

[9] M. Lange and B. Eckhardt, Vortex pairs in viscoelastic Couette-Taylor flow, Physical Review E **64**, 027301 (2001).

[10] D. G. Thomas, R. Sureshkumar, and B. Khomami, Pattern Formation in Taylor-Couette Flow of Dilute Polymer Solutions: Dynamical Simulations and Mechanism, Physical Review Letters **97**, 054501 (2006).

[11] N. Latrache, N. Abcha, O. Crumeyrolle, and I. Mutabazi, Defect-mediated turbulence in ribbons of viscoelastic Taylor-Couette flow, Physical Review E **93**, 043126 (2016).

[12] A. Groisman and V. Steinberg, Couette-Taylor Flow in a Dilute Polymer Solution, Physical Review Letters **77**, 1480 (1996).

[13] C. S. Dutcher and S. J. Muller, Effects of moderate elasticity on the stability of co- and counter-rotating Taylor–Couette flows, Journal of Rheology **57**, 791 (2013).

[14] N. Liu and B. Khomami, Elastically induced turbulence in Taylor–Couette flow: direct numerical simulation and mechanistic insight, Journal of Fluid Mechanics **737**, R4 (2013).

[15] J. D. Ferry, *Viscoelastic Properties of Polymers* (John Wiley & Sons, 1980).

[16] J. J. J. Gillissen, N. Cagney, T. Lacassagne, A. Papadopoulou, S. Balabani, and H. J. Wilson, Taylor-Couette instability in disk suspensions: Experimental observation and theory, Physical Review Fluids **5**, 083302 (2020).

[17] N. Cagney and S. Balabani, Taylor-Couette flow of shear-thinning fluids, Physics of Fluids **31**, 053102 (2019).

[18] C. S. Dutcher and S. J. Muller, Spatio-temporal mode dynamics and higher order transitions in high aspect ratio Newtonian Taylor–Couette flows, Journal of Fluid Mechanics **641**, 85 (2009).

[19] J. Gillissen, Two-Dimensional Decaying Elastoinertial Turbulence, Physical Review Letters **123**, 144502 (2019).

[20] P. R. Fenstermacher, H. L. Swinney, and J. P. Gollub, Dynamical instabilities and the transition to chaotic Taylor vortex flow, Journal of Fluid Mechanics **94**, 103 (1979).

[21] G. S. Lewis and H. L. Swinney, Velocity structure functions, scaling, and transitions in high-Reynolds-number Couette-Taylor flow, Physical Review E **59**, 5457 (1999).

[22] M. Q. Nguyen, A. Delache, S. Simoëns, W. J. T. Bos, and M. EL Hajem, Small scale dynamics of isotropic viscoelastic turbulence, Physical Review Fluids **1**, 083301 (2016).

[23] S. Sid, V. E. Terrapon, and Y. Dubief, Two-dimensional dynamics of elasto-inertial turbulence and its role in polymer drag reduction, Physical Review Fluids **3**, 011301 (2018).

[24] R. B. Bird, R. C. Armstrong, and O. Hassager, *Dynamics of polymeric liquids. Vol. 1, 2nd Ed. : Fluid mechanics*, john wiley and sons inc ed. (New York, NY, 1987).